Clustering of floating tracer due to mesoscale vortex and submesoscale fields

Dmitry V. Stepanov[1], Eugene A. Ryzhov[1], Alexei A. Zagumennov[3], Pavel Berloff[2], Konstantin V. Koshel[1]

[1]V.I.Il'ichev Pacific Oceanological Institute of FEB RAS, 43, Baltiyskaya Street, Vladivostok, 690041, Russia
[2]Department of Mathematics, Imperial College London, London, SW7 2AZ, United Kingdom
[3]Institute of Automation and Control Processes FEB RAS, 5, Radio Street, Vladivostok, 690041, Russia

Key Points:

- Phenomenology of floating tracer clustering in the divergent submesoscale and mesoscale flow;
- Exponential clustering process is analyzed depending on the submesoscale model characteristics.
- It is argued that the 2D velocity field divergence is essential for studying tracer transport properties.

Corresponding author: Dmitry Stepanov, step-nov@poi.dvo.ru

This article has been accepted for publication and undergone full peer review but has not been through the copyediting, typesetting, pagination and proofreading process, which may lead to differences between this version and the Version of Record. Please cite this article as doi: 10.1029/2019GL086504

Abstract

Floating tracer clustering is studied in oceanic flows that combine both a field of coherent mesoscale vortices, as simulated by a regional, comprehensive, eddy-resolving general circulation model, and kinematic random submesoscale velocity fields. Both fields have rotational and divergent velocity components, and depending on their relative contributions, as well as on the local characteristics of the mesoscale vortices, we identified different clustering scenarios. We found that the mesoscale vortices do not prevent clustering but significantly modify its rate and spatial pattern. We also demonstrated that even weak surface velocity divergence has to be taken into account to avoid significant errors in model predictions of the floating tracer patterns. Our approach combining dynamically constrained and random velocity fields, and the applied diagnostic methods, are proposed as standard tools for analyses and predictions of floating tracer distributions, both in observational data and general circulation models. **Plain language summary**

The problem of dispersion and aggregation of various tracers in the ocean has recently attracted a lot of interest. These tracers can be natural ocean water characteristics, such as temperature and salinity, or various hazardous impurities, such as plastic pollution and oil spills. The latter tracers are also the floating ones, which means that their dynamics is different from the passive tracers. An important and interesting aspect of the floating tracers is their ability to form pronounced clusters, that is aggregations in isolated patches — understanding and predicting this phenomenon is one of the challenges in modern oceanography. In this study we explore how floating-tracer clustering depends on kinematic characteristics of the ocean surface velocity.

1 Introduction

Mesoscale eddies are a ubiquitous component of the ocean circulation that significantly contributes to the material transport of oceanic properties and tracers, such as density, salinity, marine life and pollution. The corresponding background literature is immense, and the theoretical aspects are comprehensively reviewed in (McWilliams, 2008; Samelson, 2013). For the purposes of this study, we note that coherent mesoscale vortices constitute substantial part of the total eddy field (Barbosa Aguiar, Peliz, & Carton, 2013; Chelton, Schlax, & Samelson, 2011; Chelton, Schlax, Samelson, & de Szoeke, 2007; Martínez-Moreno, Hogg, Kiss, Constantinou, & Morrison, 2019), contribute significantly to the material transport, and are remarkably long-lived and structurally organized, as opposed to more random and wave-like eddies around them.

Ocean circulation at the scales smaller than the mesoscale is dominated by the broad range of submesoscale processes, which have been intensively studied (Berta, Griffa, Özgökmen, & Poje, 2016; Berti, Santos, Lacorata, & Vulpiani, 2011; Haza, Özgökmen, & Hogan, 2016; Huntley, Lipphardt Jr., Jacobs, & Kirwan Jr., 2015; Jacobs et al., 2016; McWilliams, 2016; Ohlmann, Romero, Palls-Sanz, & Perez-Brunius, 2019; Schroeder et al., 2012; Zhong & Bracco, 2013). Interactions between submesoscale and mesoscale motions are essential in the formation and breakdown of coherent mesoscale vortices, but the theoretical understanding is hindered by overwhelming computational costs due to the spatial resolution requirements (Dauhajre, McWilliams, & Renault, 2019). An efficient way (though, with obvious limitations) to study these interactions is by employing kinematic models for submesoscales, whereas retaining dynamical models for mesoscales — this is the approach adopted in our study and applied to the tracer clustering phenomena.

Although, it is well-established that floating tracers tend to form spatially localised aggregations (Cozar et al., 2014; Law et al., 2010; Martinez, Maamaatuaiahutapu, & Taillandier, 2009; Maximenko, Hafner, & Niiler, 2012; McComb, 1990; Okubo, 1980; Väli, Zhurbas, Laanemets, & Lips, 2018) referred to as *clusters*, their definitions and measures of the degree of clustering differ substantially (Huntley et al., 2015; Jacobs et al., 2016).

Dynamics of *floating* tracers is fundamentally different from the dynamics of *passive* tracers, because in the former case the tracer density on fluid particles changes due to the experienced surface-velocity divergence, whereas in the latter case it is materially conserved and only advected by the flow. In other words, the floating-tracer density is compressible and can not be fully described by concentrations of Lagrangian particles — this fundamental theoretical issue escaped attention of many previous studies that dealt with the Lagrangian transport on the ocean surface (Cedarholm, Rypina, Macdonald, & Yoshida, 2019; Olascoaga et al., 2013; Prants, Budyansky, & Uleysky, 2018; Wang, Olascoaga, & Beron-Vera, 2015). Physical mechanisms leading to formation of clusters can be different and overall remain poorly understood. This study deals with clustering due to the surface-velocity divergence, which is present in both mesoscale and submesoscale motions.

We focus on tracers *floating* on the ocean surface and, therefore, directly experiencing only the 2D surface velocity. We define clusters as small and transient areas that exponentially shrink in time and collect the exponentially growing in time fraction of the tracer (Isichenko, 1992; Klyatskin & Koshel, 2000). The asymptotic theory of clustering in random velocity fields (Klyatskin, 2015) states that the exponential clustering occurs necessarily, if the divergent velocity component completely dominates over the rotational one. When both components are comparable, the exponential clustering persists but its properties become significantly altered (Koshel, Stepanov, Ryzhov, Berloff, & Klyatskin, 2019) — this result is, however, restricted to specific and purely kinematic velocities. The main novelty of the present work is in relaxing this restriction by dynamically constraining the mesoscale flow component, which is referred to as the regular component. The random velocity field modelling the submesoscales represents $\sim 200-2000$ m scales, has the surface divergence, which is 2 orders of magnitude larger than that of the mesoscales, is controlled by only 2 parameters: correlation radius and variance.

This Letter aims at establishing phenomenology of possible floating-tracer clustering scenarios depending on the submesoscale divergent flow component in the presence of dynamically modeled coherent mesoscale vortices.

2 Models

In this section we discuss the submesoscale and mesoscale velocity models, and how the tracer density fields were obtained.

Floating tracer is advected by a 2D flow with velocity $\mathbf{U}(\mathbf{R},t) = (u(\mathbf{r},t), v(\mathbf{r},t))\,|_{z=0}$ characterized by the divergence

$$\nabla_{\mathbf{R}}\mathbf{U}(\mathbf{R},t) = -\frac{\partial w(\mathbf{r},t)}{\partial z}\,|_{z=0}\ , \tag{1}$$

where $\mathbf{r} = (x,y,z)$ is the full position vector; $\mathbf{R} = (x,y)$ is the horizontal position vector; $\nabla_{\mathbf{R}}\mathbf{U}(\mathbf{R},t)$ is the horizontal divergence at the ocean surface ($z = 0$); and $w(\mathbf{r},t)$ is the vertical velocity component.

Since there is no vertical flux of the floating tracer, the evolution of its density $\rho(\mathbf{r},t)$ is governed by the conservation law:

$$\left(\frac{\partial}{\partial t} + \nabla_{\mathbf{R}}\mathbf{U}(\mathbf{R},t)\right)\rho(\mathbf{R},t) = 0\,, \qquad \rho(\mathbf{R},0) = \rho_0(\mathbf{R})\,, \tag{2}$$

and the total mass of the tracer is conserved: $M = \int d\mathbf{R}\rho(\mathbf{R},t) = const$. We treat (2) and the velocity field in a nondimensional form, with the space, time and density scales denoted as L_0, t_0 and ρ^*, respectively, and chosen to be the typical mesoscale eddy size (i.e., of the order of the first baroclinic Rossby radius) and turnover time, and the initial density (distributed over the unity size area); and the velocity scale follows from this as $U^* = L_0/t_0$.

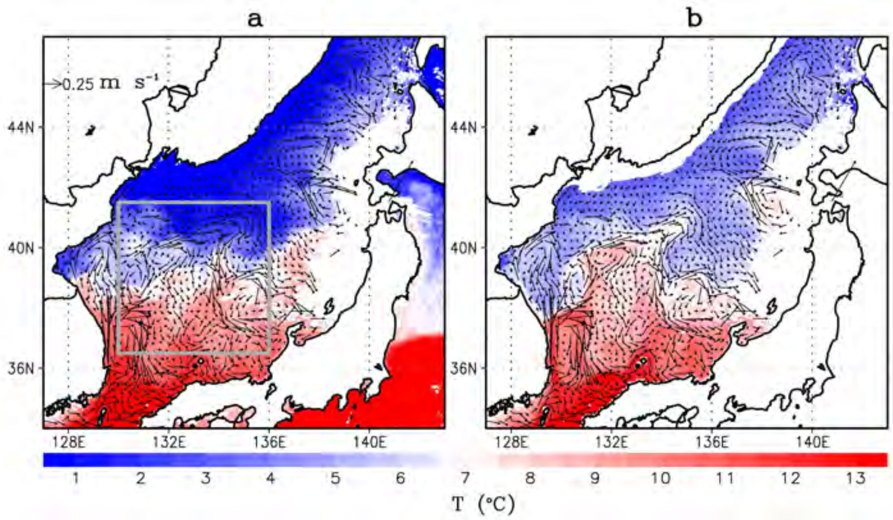

Figure 1: Monthly mean (March 2000) sea surface mesoscale velocity field (regular component) from the Japan/East Sea circulation model; the corresponding monthly mean sea surface temperature (colour shading, in degrees of Celsius) from (a) satellite observations and (b) model. The general circulation patterns are reliably captured by the simulation, so that the warm and cold regions of the JES are separated by the intense meandering jet and its adjacent vortices. The grey square indicates the subdomain of interest.

2.1 Mesoscale velocity model

The mesoscale (regular) component is a solution of an eddy-resolving (1/12-degree), regional, hydrostatic Boussinesq, sigma-coordinate, INMOM model (Diansky, Stepanov, Gusev, & Novotryasov, 2016; Stepanov, Diansky, & Novotryasov, 2014) configured for the Japan/East Sea (JES) region plus the Sea of Okhotsk and adjacent parts of the Pacific Ocean. It is driven by the atmospheric forcing provided by the JRA55-do dataset covering the 1958−2017 period, and incorporating climatological boundary conditions on the open boundaries of the domain (Stepanov, Diansky, & Fomin, 2018). The simulated solution is averaged over one-month intervals (Fig. 1b), and one of its surface velocity snapshots (March 2000) in the south-western JES region is used for the follow-up analyses. To validate the simulated velocity field, we overlaid it with the corresponding monthly mean sea surface temperature (SST) data provided by the AVHRR (Advanced Very-High-Resolution Radiometer) mounted on the satellites NOAA-12 and NOAA-15. The simulated circulation of the JES is consistent with the existing observations (Diansky et al., 2016; Stepanov et al., 2014).

We picked up the subdomain containing pronounced vortices with horizontal shears (grey square in Fig. 1 corresponds to the vorticity field (left panel) and the divergence field (right panel) in Fig. 2). The locations of interest, designated (Fig. 2) by C_1 (cyclonic eddy), A_2 (two weak anticyclonic eddies) and A_1 (cyclone and anticyclone pair), serve as typical eddy configurations with their distinct material transport patterns. At this stage we are interested in clustering phenomena developing much faster than the characteristic time scale of the mesoscale (regular) velocity field — this justifies our use of the stationary mesoscale flow.

In dimensional units, the random velocity scale is 2.0 m/s, whilst the characteristic regular velocity is of the order of magnitude smaller, i.e., about 0.2 m/s. The characteristic divergence of the regular velocity is about 10^{-6} s^{-1} (see the top-right panel

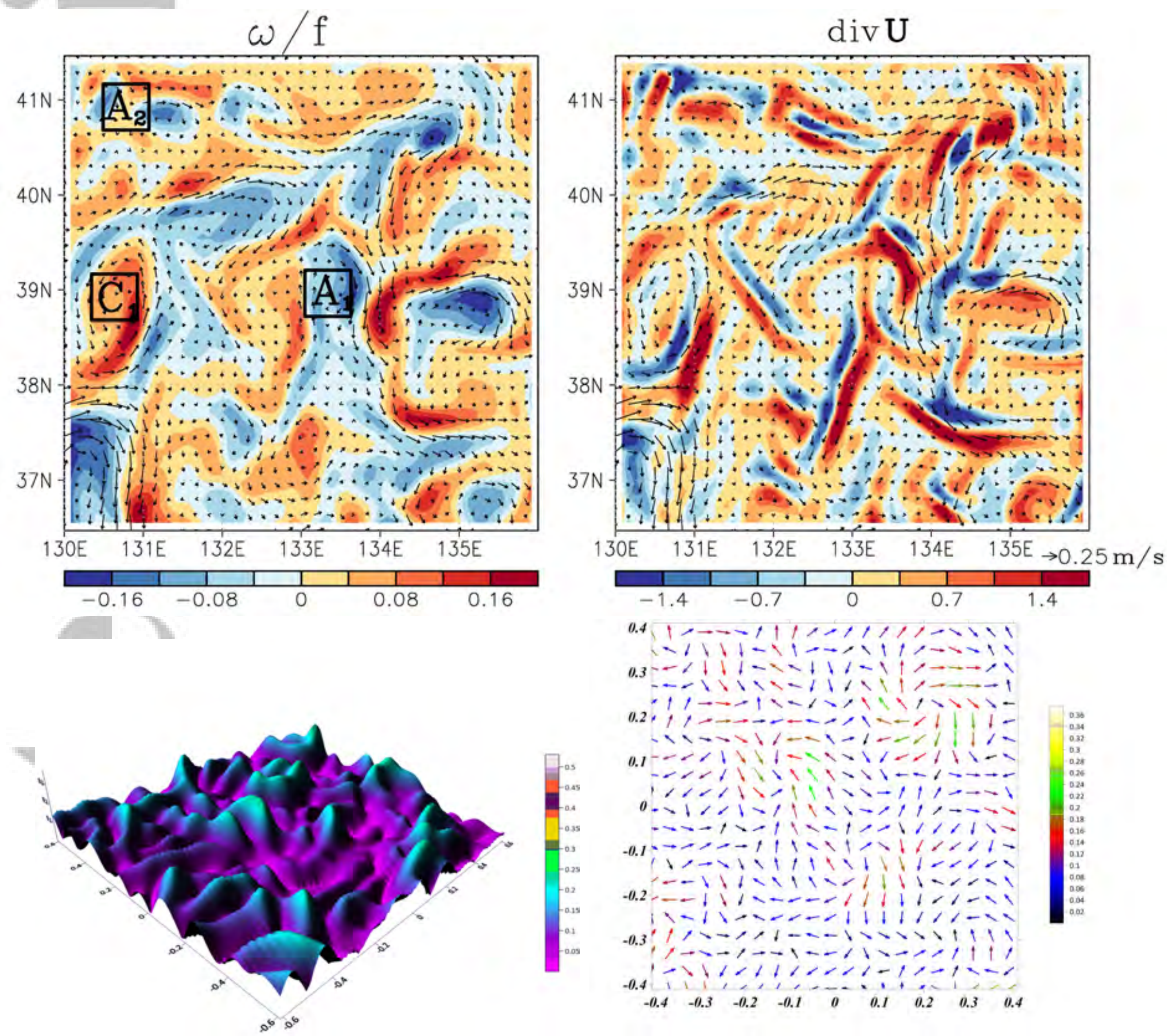

Figure 2: Top row: regular (mesoscale) flow fields. Left panel: vertical component of the relative vorticity vector normalized by the local Coriolis parameter; right panel: surface-velocity divergence (units are $10^{-6}s^{-1}$). The squares labelled as A_1, A_2 and C_1 denote the tracer deployment regions. Bottom row: snapshots of the random flow properties in a zoomed in subdomain, and for $\gamma = 0.5$. Left panel: the corresponding flow speed; right panel: the corresponding random velocity field (color-coded).

in Fig. 2), whilst the random velocity divergence is orders of magnitude larger, i.e., about $10^{-2}\ s^{-1}$.

2.2 Submesoscale velocity model

The 2D divergent velocity field $\mathbf{U}$ is random, normally distributed, spatially homogeneous, isotropic, and stationary; it is also a linear combination of the modelled mesoscale mean, and the submesoscale divergent and rotational components:

$$\mathbf{U}(\mathbf{R},t) = \underbrace{\langle \mathbf{U}(\mathbf{R},t)\rangle}_{\textbf{mesoscale}} + \underbrace{\gamma \mathbf{U}^p(\mathbf{R},t) + (1-\gamma)\mathbf{U}^s(\mathbf{R},t)}_{\textbf{submesoscale}}, \tag{3}$$

where superscript p indicates the divergent (irrotational) component, superscript s indicates the rotational (nondivergent) component, and parameter $0 \le \gamma \le 1$ sets their relative contributions.

Our next goal is to formulate a model for random, spatially correlated, and temporally uncorrelated (i.e., δ-correlated), kinematic velocity field; for this purpose we define (Klyatskin, 1994, 2015) the correlation tensor:

$$B^j_{\alpha\beta}(\mathbf{R}',\eta) = \langle U^j_\alpha(\mathbf{R},t) U^j_\beta(\mathbf{R}+\mathbf{R}',t+\eta)\rangle = \int d\mathbf{k} E^j_{\alpha\beta}(\mathbf{k},\eta) e^{i\mathbf{k}\mathbf{R}'}, \tag{4}$$

where indices α and β stand for x and y and indicate different components of the tensor; and index j stands for p and s, and indicates different tensors; and the following spectral densities are assumed:

$$E^p_{\alpha\beta}(\mathbf{k},\eta) = E^p(k,\eta)\frac{k_\alpha k_\beta}{k^2}, \qquad E^s_{\alpha\beta}(\mathbf{k},\eta) = E^s(k,\eta)\left(\delta_{\alpha\beta} - \frac{k_\alpha k_\beta}{k^2}\right). \tag{5}$$

The correlation tensor is nonzero only for the zero time lag η:

$$B^j_{\alpha\beta}(\mathbf{0},0) = \langle U^j_\alpha(\mathbf{R},t) U^j_\beta(\mathbf{R},t)\rangle = \frac{1}{2}\left(\sigma^j_{\mathbf{U}}\right)^2 \delta_{\alpha\beta}, \tag{6}$$

where $\left(\sigma^j_{\mathbf{U}}\right)^2 = B^j_{\alpha\alpha}(\mathbf{0},0) = \int d\mathbf{k} E^j(k,0)$. In our case we take $E^s = E^p = E$, and the spectral density is taken as

$$E(k,0;l) = \frac{1}{2\pi}\frac{l^4}{4}k^2 \exp\left\{-\frac{1}{2}k^2 l^2\right\}, \tag{7}$$

where l is the spatial correlation radius parameter. In numerical simulations, we use random phase, $\sigma^p_{\mathbf{U}} = \sigma^s_{\mathbf{U}} \simeq 0.1$, which results in the typical velocity of 0.2 m/s, $l = 0.08$ (i.e., 2.0 km), and time step 0.01 (i.e., 120 s).

2.3 Numerical implementation and methodology

We simulated the random velocity spectrally on uniform 2048×2048 grid (Klyatskin & Koshel, 2017), and the regular velocity component is taken to be piecewise-constant over the same grid. Since the random field is not differentiable in time, we solve the Lagrangian equivalent of (2),

$$\begin{aligned} \frac{d\mathbf{R}}{dt} &= \mathbf{U}(\mathbf{R},t),\ \mathbf{R}(0) = \xi, \\ \frac{d\rho}{dt} &= -\nabla_{\mathbf{R}}\mathbf{U}(\mathbf{R},t)\rho(t),\ \rho(0) = \rho_0(\xi), \end{aligned} \tag{8}$$

as applied to ensembles of Lagrangian particles advected by the total velocity field and solved numerically by the method of characteristics (Klyatskin, 1994, 2015; Koshel & Alexandrova, 1999), where ξ is the initial position of each particle. Equations (8) are time-stepped using the standard Euler-Itô scheme (Kloeden & Platen, 1992; Klyatskin & Koshel, 2017; Koshel & Alexandrova, 1999), and the Eulerian density field can be obtained by the spatial coarse-graining, if needed.

To analyze the clustering we employed the statistical topography methodology (Isichenko, 1992). One of the characteristics used in statistical topography is the *clustering area*, which is defined as the total combined area of the regions where the tracer density exceeds certain threshold:

$$\langle S(t;\bar{\rho})\rangle = \int d\mathbf{R}\ \langle \theta(\rho(\mathbf{R},t)-\bar{\rho})\rangle = \int d\mathbf{R} \int_{\bar{\rho}}^{\infty} d\rho'\, P(\mathbf{R},t;\rho')\,, \tag{9}$$

where $\theta\,(\cdot)$ is the Heaviside (step) function; and $P(\mathbf{R},t;\rho)$ is the probability density function (PDF) of the tracer density. The other useful characteristics is the *clustering mass*, which is the amount of tracer aggregated within the clustering area:

$$\langle M(t;\bar{\rho})\rangle = \int d\mathbf{R}\,\rho(\mathbf{R},t)\,\langle \theta(\rho(\mathbf{R},t)-\bar{\rho})\rangle = \int d\mathbf{R} \int_{\bar{\rho}}^{\infty} d\rho'\,\rho' P(\mathbf{R},t;\rho')\,. \tag{10}$$

In the exponential clustering regime, the clustering area tends to zero, and the clustering mass tends to unity (i.e., clusters accumulate all the available tracer) in the large-time limit (Klyatskin, 2015; Klyatskin & Koshel, 2017). The exact analytical estimates for the clustering area and mass are derived in (Klyatskin, 2015) for purely divergent velocity case:

$$\langle S(t;\bar{\rho})\rangle \sim exp(-\frac{1}{4}\tau)/\sqrt{\tau} = exp(-\frac{1}{4}D_p t)/\sqrt{D_p t}, \qquad \langle M(t;\bar{\rho})\rangle \sim 1-\langle S(t;\bar{\rho})\rangle\ , \tag{11}$$

where $D_p = (\gamma^2\sigma_U^2/l^2)t_0$ is the effective diffusivity of the divergent velocity component. Most of our numerical simulations were carried out with $\sigma_U = 0.1$ and $l = 0.08$; and for this set of parameters, we use notation D_0 instead of D_p.

We distribute 3 square-shaped tracer patches in the subdomain of interest (Fig. 2), and each tracer patch contains 36×10^6 uniformly distributed Lagrangian particles. This number of particles has been tested (by doublind and halving) and found adequate in capturing the clustering characteristics of interest; moreover, when we considered a purely divergent and no-mean velocity field ($\gamma = 1$), the numerical solution matched the corresponding asymptotic estimate (11). Four experiments have been devised with the same regular velocity and different random velocity fields:

1. EXP1 employs only the regular velocity field and forms the reference solution to evaluate the effect of the submesoscale further;
2. EXP2 — plus the purely rotational random velocity field ($\gamma = 0$);
3. EXP3 — plus the purely divergent random velocity field ($\gamma = 1$);
4. EXP4 — plus the mixed random velocity field ($\gamma = 0.5$).

3 Clustering scenarios

The reference case EXP1 (i.e., with the random submesoscale component switched off) illustrates typical tracer patterns in the deployment regions (Fig. 3a). Stationary vortices retain the tracer; in the regions with no closed streamlines, the tracer is intensely stirred and spread out; large values of tracer density are rare and correspond to the sinks in the flow field.

Now, we turn our attention to the benchmark solutions (EXP2, EXP3, and EXP4) featuring different submesoscale flow components. The purely rotational EXP2 solution

(Fig. 3b) is characterized by smearing of the tracer patches due to enhanced tracer dispersion. Similar effect has been observed in the model of an isolated ellipsoidal vortex subject to random velocity perturbations (Koshel, Ryzhov, & Zhmur, 2013). Overall tracer patterns and density values are similar to EXP1 (Fig. 3a), but the boundaries of the tracer patches are more filamented due to the random fluctuations.

When the random velocity field is purely divergent (EXP3; $\gamma = 1$; Fig. 3c), the tracer evolution is characterized by the exponential clustering (followed up to the two orders of magnitude density increase). On the other hand, the overall large-scale pattern of the mesoscale-size tracer features, that is clearly seen in the other experiments, is significantly eroded. Remarkably, the exponential clustering develops even within the intensively sheared mesoscale jet and vortices (entirely from vortex peripheries to cores). Somewhat similar but grainy small-scale pattern is found when amplitudes of the rotational and divergent submesoscale flow components are equal (EXP4; $\gamma = 0.5$): the tracer evolution is also characterized by the exponential clustering (Fig. 3d), and tThe large-scale tracer distribution pattern is like in EXP1 and EXP2.

Since our interest is mostly in the clustering process subject to coherent mesoscale vortices, we choose a typical situation — the cyclone over C_1 deployment location — and analyze the corresponding tracer evolution in detail (Fig. 4). In EXP1 the tracer is expelled towards periphery of the cyclone; in EXP2 it is additionally smeared across the mesoscale shear, and the boundary of the tracer patch is significantly more distorted; in EXP3 the exponential clustering is most pronounced (Figs. 3–4); in EXP4 despite the strong influence of the rotational component, the exponential clustering still persists; qualitative difference between the clustering dynamics in EXP3 and EXP4 are discussed in the next section. Note, that clusters tend to aggregate differently in cyclones (tendency towards the periphery) and anticyclones (tendency towards the centre); e.g., consider A_1, where clusters fill up the anticyclone's centre.

For a partial interpretation of the modeling results, we resort to the asymptotic theory of clustering in random velocity fields containing uniform-shear flow component (Klyatskin, 2015), which predicts the following time dependence of the single-particle dispersion:

$$\sigma_{xx}^2 = 2D_0 t(1 + \alpha t + \frac{1}{3}\alpha^2 t^2)\,, \qquad \sigma_{yy}^2 = 2D_0 t\,, \tag{12}$$

where α is the shear parameter. According to this estimate, a tracer patch should be smeared in time, and more so along the shear direction (Fig. 3b); but in the case of purely rotational velocity (i.e., there is no exponential clustering), there is an estimate for the dispersion of the density gradient p (Klyatskin, 2015):

$$\left\langle p^2\left(t\right)\right\rangle \sim \exp\left\{\left(\frac{3}{2}\alpha^2 D_s\right)^{1/3} t\right\}\,, \tag{13}$$

where D_s is the variation due to the purely rotational random velocity field. This estimate is obtained in the limit $D_s \ll \alpha$, when $\alpha \neq 0$, and its interpretation is as follows: regardless of how small D_s is, it still contributes towards increasing the gradient dispersion, that is, it makes the tracer patch boundary more serrated (similar tendencies are seen in Fig. 3b), opposite to the (elongating) effect of uniform shear on the tracer patch. Although, the above estimate is valid for uniform shear, we expect it to be true for more complicated shears, and this expectation is consistent with the solutions discussed in this section.

To quantify clustering properties in the above-discussed scenarios, we make use of statistical topography diagnostics, such as the clustering area and mass. In EXP4 the rate of exponential clustering (Fig. 5) is qualitatively similar to but still slower to the theoretical prediction for the purely divergent case EXP3 (Klyatskin, 2015; Klyatskin & Koshel, 2017; Koshel et al., 2019). Despite the general tendency towards the exponential clustering, the clustering process is significantly affected by the specifics of the

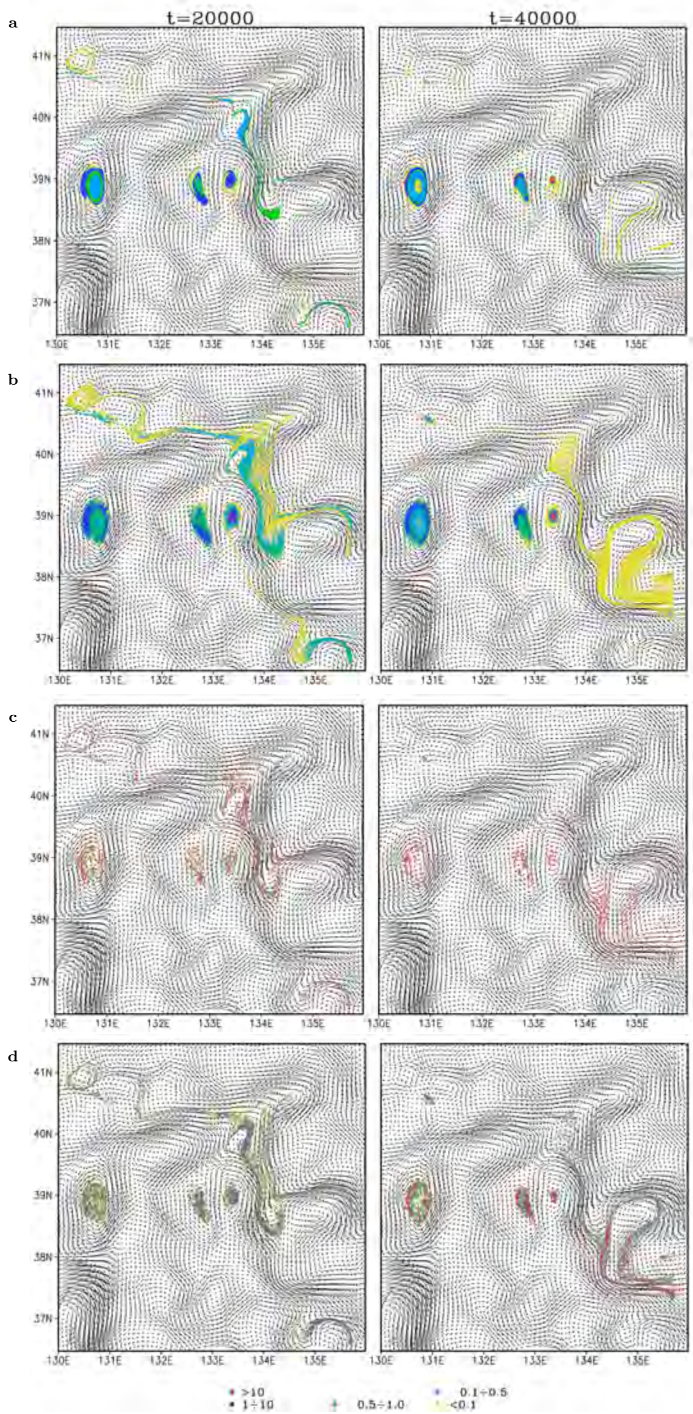

Figure 3: Tracer densities corresponding to (a) EXP1 – regular velocity component, no random velocity, (b) EXP2 – regular plus purely rotational random velocity component, (c) EXP3 – regular plus purely divergent random velocity component, and (d) EXP4 – regular plus mixed rotational and divergent random velocity components ($\gamma = 0.5$)). Colour-coded is the dimensionless tracer density; red values indicate the exponential clustering. The tracer advection patterns remain similar: the C_1-tracer remains bounded to the original deployment site; the A_1-tracer is redistributed within the cyclone-anticyclone pair; the A_2-tracer is advected southeastward.

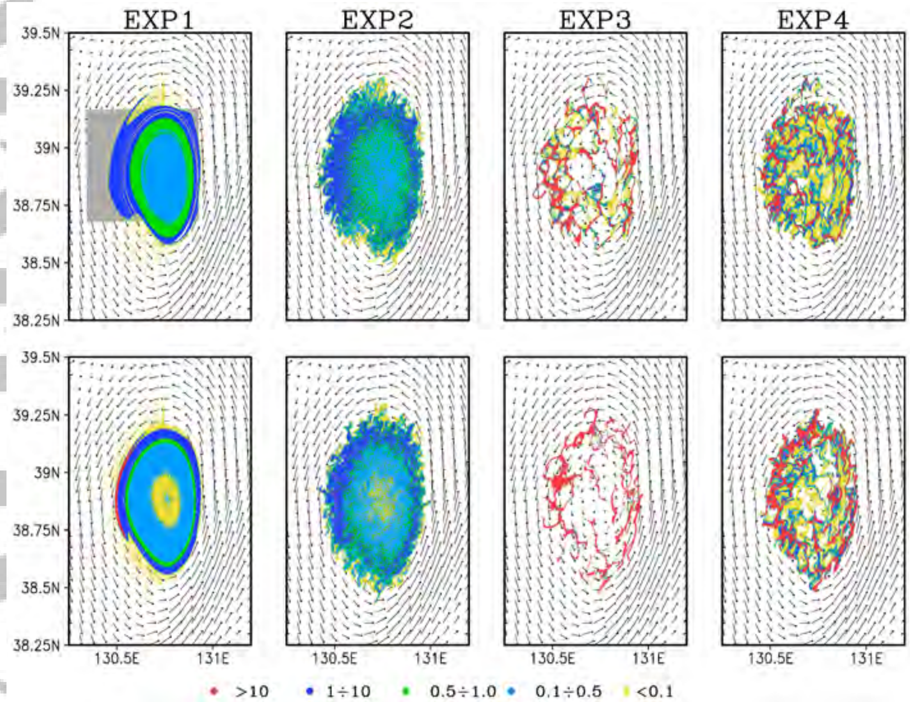

Figure 4: Tracer density for the benchmark experiments. The enlarged region corresponds to C_1 deployment location. Top and bottom rows correspond to consequent dimensionless time instances $t = 20000$ and 40000, respectively. The rest is as in Fig. 2.

regular velocity, as illustrated by different evolution curves for different locations of the initial tracer deployment (Fig. 5). Formation of clusters can be inhibited by intense shear in jet-like flows, as can be seen in Fig. 5 for the A_2 case.

Changing the random velocity field parameters σ_U and l is similar to changing the diffusivity. The clustering proxy curves calculated for different sets of the parameters (purple curve ($\sigma_U = 0.2, l = 0.04$), thin black curve ($\sigma_U = 0.1, l = 0.16$) and other combinations in fig. 5) produce similar shapes of the curves. If D_p is decreased, the clustering rate slows down for the larger values of the clustering mass (Jacobs et al., 2016); if D_p is increased, the rate of clustering in the large-time limit decreases; overall, the effective diffusivity cannot stop or initiate clustering, and only modifies it.

4 Conclusions

This study was motivated by the well-established phenomenon of clustering, that is, the development of spatially localised aggregations, here, of floating tracers (e.g., marine plastic or other pollution, marine biomass) on the ocean surface. The underlying theory for this phenomenon remains largely undeveloped, except for simple kinematic, random velocity flows, which are our starting point. The work contributes to a better understanding of the effects characteristic of the floating tracer as compared to the passive one. The other novelty is in considering clustering in the velocity field containing both random and regular (i.e., dynamically constrained) components. The latter component comes from a dynamical, realistic, general circulation model of the Japan/East Sea's region, and it features mesoscale vortices; the former one aims at representing submesoscale motions unresolved by the dynamical model and simulated by a random kinematic model.

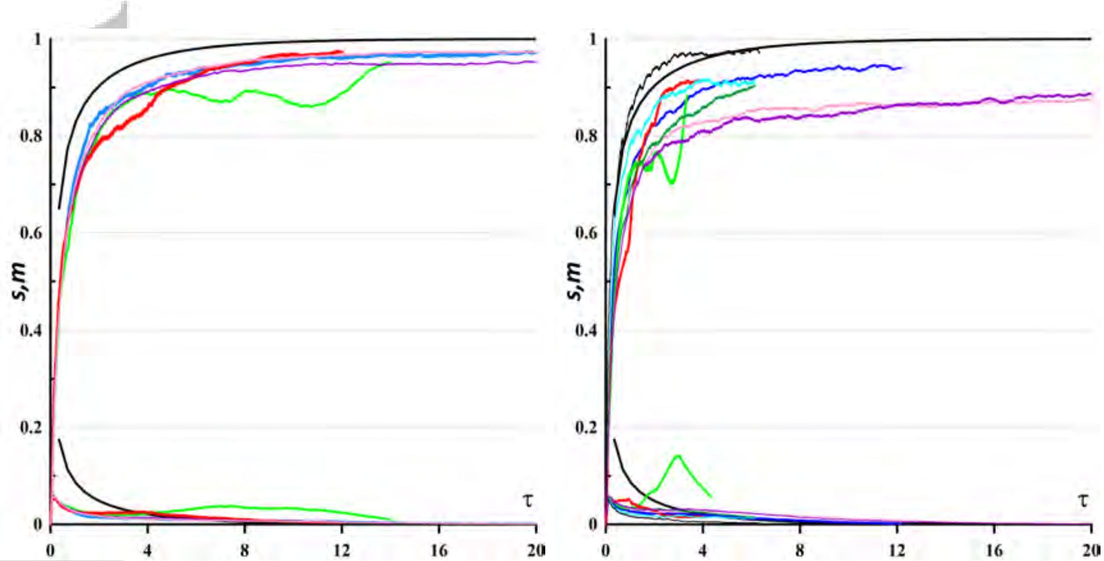

Figure 5: Time series of clustering mass (top curves) and clustering area (bottom curves) for EXP3 (left panel) and EXP4 (right panel) for the tracer deployment locations: C_1 - blue lines, A_1 - red lines, and A_2 - green lines ($\sigma_U = 0.1, l = 0.08$). The black curves show theoretical estimates (11) for the purely divergent case (EXP3). Additional curves correspond to different sets of the parameters (σ_U, l) through (11), and the tracer deployment location C_1: purple – $D_p = 16D_0$ ($\sigma_U = 0.2, l = 0.04$); thin black – $D_p = \frac{1}{4}D_0$ ($\sigma_U = 0.1, l = 0.16$); light blue – $D_p = D_0$ ($\sigma_U = 0.2, l = 0.16$); pink – $D_p = 4D_0$ ($\sigma_U = 0.1, l = 0.04$); dark green – $D_p = D_0$ ($\sigma_U = 0.05, l = 0.04$)). For most of the cases, the exponential nature of clustering is clearly evident.

Four experiments with gradually increased influence of the divergent component of the flow were devised; 3 regions of interest were selected, as represented by typical footprints of the mesoscale eddies: an isolated cyclonic eddy; two anticyclonic eddies; a pair of cyclonic-anticyclonic eddies. A compelling feature of the presented clustering behaviour is the widespread distribution of intermittent patterns of floating-tracer clusters within regions of intense shears, such as vortices and jets. This suggests that real mesoscale eddies in the ocean should also contain similar patterns; although, the relevant observations are either scarce or with inadequate spatial resolution (see Fig. 1 in (Huntley et al., 2015) and Fig. 2 in (Lim et al., 2012), which feature intermittent cluster patterns similar to our model solutions).

Upon comparison with the comprehensive study (Jacobs et al., 2016), we agree with their scenario that the short-time clustering is associated with the submesoscale divergence but argue that the long-term clustering is also due to the submesoscale divergence, while the mesoscales do not directly induce clustering but rather advect already formed clusters into larger aggregations. This is asserted using the statistical topography techniques showing that the rate of clustering does not change in time and is largely independent of the spatial inhomogeneities, such as given by mesoscale eddies.

A serious challenge for further comparison between the model solution and observations is disentangling of specific contributions of the rotational and divergent velocity components that are shown to be essential for the rate and intensity of the clustering process.

Acknowledgments

This study was partially supported by the POI FEB RAS Program “Mathematical simulation and analysis of dynamical processes in the ocean” ($AAAA-A117030110034-7$) and by the Russian Foundation for Basic Research projects $19-55-10001$, $20-05-00083$. EAR and PB were supported by the NERC grant $NE/R011567/1$ and by the Royal Society Exchange Grant $IEC/R2/181033$. The contribution of KVK in obtaining the analytical estimates was supported by the Russian Scientific Foundation project $19-17-00006$. PB also gratefully acknowledges support from the NERC grant $NE/T002220/1$ and the Leverhulme grant $RPG-2019-024$, as well as the hospitality of the Shirshov Institute of Oceanology. The numerical simulation outputs were obtained using the Shared Resource Center “Far Eastern Computing Resource” IACP FEB RAS (`https://www.cc.dvo.ru`). Data are available `https://www.researchgate.net/publication/336133063_dataset_for_Geophysical_Research_Letters`.

References

Barbosa Aguiar, A. C., Peliz, A., & Carton, X. (2013). A census of meddies in a long-term high-resolution simulation. *Prog. Oceanogr.*, *116*, 80–94. doi: 10.1016/j.pocean.2013.06.016

Berta, M., Griffa, A., Özgökmen, T. M., & Poje, A. C. (2016). Submesoscale evolution of surface drifter triads in the gulf of mexico. *Geophys. Res. Lett.*, *43*(22), 11,751–11,759. doi: 10.1002/2016GL070357

Berti, S., Santos, F. A. D., Lacorata, G., & Vulpiani, A. (2011). Lagrangian drifter dispersion in the southwestern atlantic ocean. *J. Phys. Oceanogr.*, *41*(9), 1659–1672. doi: 10.1175/2011JPO4541.1

Cedarholm, E. R., Rypina, I. I., Macdonald, A. M., & Yoshida, S. (2019). Investigating subsurface pathways of fukushima cesium in the northwest pacific. *Geophys. Res. Lett.*, *46*(12), 6821-6829. doi: 10.1029/2019GL082500

Chelton, D. B., Schlax, M. G., & Samelson, R. M. (2011). Global observations of nonlinear mesoscale eddies. *Prog. Oceanogr.*, *91*(2), 167–216.

Chelton, D. B., Schlax, M. G., Samelson, R. M., & de Szoeke, R. A. (2007). Global observations of large oceanic eddies. *Geophys. Res. Lett.*, *34*, L15606.

Cozar, A., Echevarria, F., Gonzalez-Gordillo, J. I., Irigoien, X., Ubeda, B., Hernandez-Leon, S., ... Duarte, C. M. (2014). Plastic debris in the open ocean. *Proceedings of the National Academy of Sciences*, *111*, 10239-10244. doi: 10.1073/pnas.1314705111

Dauhajre, D. P., McWilliams, J. C., & Renault, L. (2019). Nearshore lagrangian connectivity: Submesoscale influence and resolution sensitivity. *J. Geophys. Res.: Oceans*, *124*(7), 5180–5204. doi: 10.1029/2019JC014943

Diansky, N. A., Stepanov, D. V., Gusev, A. V., & Novotryasov, V. V. (2016). Role of wind and thermal forcing in the formation of the water circulation variability in the Japan/East Sea Central Basin in 1958–2006. *Izvestiya, Atmospheric and Oceanic Physics*, *52*, 207–216. doi: 10.1134/S0001433816010023

Haza, A. C., Özgökmen, T. M., & Hogan, P. (2016). Impact of submesoscales on surface material distribution in a gulf of mexico mesoscale eddy. *Ocean Modelling*, *107*, 28 - 47. doi: https://doi.org/10.1016/j.ocemod.2016.10.002

Huntley, H. S., Lipphardt Jr., B. L., Jacobs, G., & Kirwan Jr., A. D. (2015). Clusters, deformation, and dilation: Diagnostics for material accumulation regions. *J. Geophys. Res.: Oceans*, *120*(10), 6622-6636. doi: 10.1002/2015JC011036

Isichenko, M. B. (1992). Percolation, statistical topography, and transport in random media. *Rev. Mod. Phys.*, *64*, 961–1043. doi: 10.1103/RevModPhys.64.961

Jacobs, G. A., Huntley, H. S., Kirwan Jr., A. D., Lipphardt Jr., B. L., Campbell, T., Smith, T., ... Bartels, B. (2016). Ocean processes underlying surface clustering. *Journal of Geophysical Research: Oceans*, *121*(1), 180-197. doi: 10.1002/2015JC011140

Kloeden, P., & Platen, E. (1992). *Numerical solution of stochastic differential equations*. Springer, Berlin.

Klyatskin, V. I. (1994). Statistical description of the diffusion of a passive tracer in a random velocity field. *Physics-Uspekhi*, *37*, 501–513.

Klyatskin, V. I. (2015). *Stochastic equations: Theory and applications in acoustics, hydrodynamics, magnetohydrodynamics, and radiophysics* (Vols. 1,2). Springer.

Klyatskin, V. I., & Koshel, K. (2017). Impact of diffusion on surface clustering in random hydrodynamic flows. *Phys. Rev. E*, *95*, 013109. doi: 10.1103/PhysRevE.95.013109

Klyatskin, V. I., & Koshel, K. V. (2000). The simplest example of the development of a cluster-structured passive tracer field in random flows. *Physics-Uspekhi*, *170*, 771–778.

Koshel, K. V., & Alexandrova, O. V. (1999). Some results of a numerical modeling of the diffusion of passive tracers in a random field of velocities. *Izv. Atmos. Ocean. Phys.*, *35*, 578–588.

Koshel, K. V., Ryzhov, E. A., & Zhmur, V. V. (2013). Diffusion-affected passive scalar transport in an ellipsoidal vortex in a shear flow. *Nonlin. Processes Geophys.*, *20*, 437–444. doi: 10.5194/npg-20-437-2013

Koshel, K. V., Stepanov, D. V., Ryzhov, E. A., Berloff, P., & Klyatskin, V. I. (2019). Clustering of floating tracers in weakly divergent velocity fields. *Physical Review E*, *100*. doi: 10.1103/PhysRevE.100.063108

Law, K. L., Moret-Ferguson, S., Maximenko, N. A., Proskurowski, G., Peacock, E. E., Hafner, J., & Reddy, C. M. (2010). Plastic accumulation in the north atlantic subtropical gyre. *Science*, *329*, 1185-1188. doi: 10.1126/science.1192321

Lim, J.-H., Son, S., Park, J.-W., Kwak, J. H., Kang, C.-K., Son, Y. B., ... Lee, S. H. (2012). Enhanced biological activity by an anticyclonic warm eddy during early spring in the east sea (japan sea) detected by the geostationary ocean color satellite. *Ocean Science Journal*, *47*, 377-385. doi:

10.1007/s12601-012-0035-1

Martinez, E., Maamaatuaiahutapu, K., & Taillandier, V. (2009). Floating marine debris surface drift: Convergence and accumulation toward the south pacific subtropical gyre. *Marine Pollution Bulletin*, *58*, 1347 1355.

Martínez-Moreno, J., Hogg, A. M., Kiss, A. E., Constantinou, N. C., & Morrison, A. K. (2019). Kinetic energy of eddy-like features from sea surface altimetry. *Journal of Advances in Modeling Earth Systems*, *11*(10), 3090-3105. doi: 10.1029/2019MS001769

Maximenko, N., Hafner, J., & Niiler, P. (2012). Pathways of marine debris derived from trajectories of lagrangian drifters. *Marine Pollution Bulletin*, *65*(1-3), 51–62. doi: 10.1016/j.marpolbul.2011.04.016

McComb, W. D. (1990). *The physics of fluid turbulence* (Vol. 25). Oxford: Clarendon Press.

McWilliams, J. C. (2008). The nature and consequences of oceanic eddies. In *Ocean modeling in an eddying regime* (p. 5-15). American Geophysical Union (AGU). doi: 10.1029/177GM03

McWilliams, J. C. (2016). Submesoscale currents in the ocean. *Proc. R. Soc. A*, *472*, 20160117. doi: 10.1098/rspa.2016.0117

Ohlmann, J. C., Romero, L., Palls-Sanz, E., & Perez-Brunius, P. (2019). Anisotropy in coastal ocean relative dispersion observations. *Geophys. Res. Lett.*, *46*(2), 879–888. doi: 10.1029/2018GL081186

Okubo, A. (1980). *Diffusion and ecological problems: Mathematical models* (Vol. 10). Berlin: Springer-Verlag.

Olascoaga, M. J., Beron-Vera, F. J., Haller, G., Trinanes, J., Iskandarani, M., Coelho, E. F., ... Valle-Levinson, A. (2013). Drifter motion in the Gulf of Mexico constrained by altimetric Lagrangian coherent structures. *Geophys. Res. Lett.*, *40*, 6171–6175. doi: 10.1002/2013GL058624

Prants, S. V., Budyansky, M. V., & Uleysky, M. Y. (2018). How eddies gain, retain, and release water: A case study of a hokkaido anticyclone. *J. Geophys. Res.: Oceans*, *123*(3), 2081-2096.

Samelson, R. M. (2013). Lagrangian motion, coherent structures, and lines of persistent material strain. *Annu. Rev. Mar. Sci.*, *5*, 137–163. doi: 10.1146/annurev-marine-120710-100819

Schroeder, K., Chiggiato, J., Haza, A. C., Griffa, A., Özgökmen, T. M., Zanasca, P., ... Trees, C. (2012). Targeted lagrangian sampling of submesoscale dispersion at a coastal frontal zone. *Geophys. Res. Lett.*, *39*(11). doi: 10.1029/2012GL051879

Stepanov, D. V., Diansky, N. A., & Fomin, V. V. (2018). Eddy energy sources and mesoscale eddies in the Sea of Okhotsk. *Ocean Dynamics*, *68*, 825 – 845. doi: 10.1007/s10236-018-1167-3

Stepanov, D. V., Diansky, N. A., & Novotryasov, V. V. (2014). Numerical simulation of water circulation in the central part of the Sea of Japan and study of its long-term variability in 1958–2006. *Izvestiya, Atmospheric and Oceanic Physics*, *50*, 73–84. doi: 10.1134/S0001433813050149

Väli, G., Zhurbas, V. M., Laanemets, J., & Lips, U. (2018). Clustering of floating particles due to submesoscale dynamics: a simulation study for the gulf of finland, baltic sea. *Fundamentalnaya i Prikladnaya Gidrofizika*, *11*(2), 21-35. doi: 10.7868/S2073667318020028

Wang, Y., Olascoaga, M. J., & Beron-Vera, F. J. (2015). Coherent water transport across the south atlantic. *Geophys. Res. Lett.*, *42*(10), 4072-4079. doi: 10.1002/2015GL064089

Zhong, Y., & Bracco, A. (2013). Submesoscale impacts on horizontal and vertical transport in the gulf of mexico. *J. Geophys. Res.: Oceans*, *118*(10), 5651–5668. doi: 10.1002/jgrc.20402

fig1.

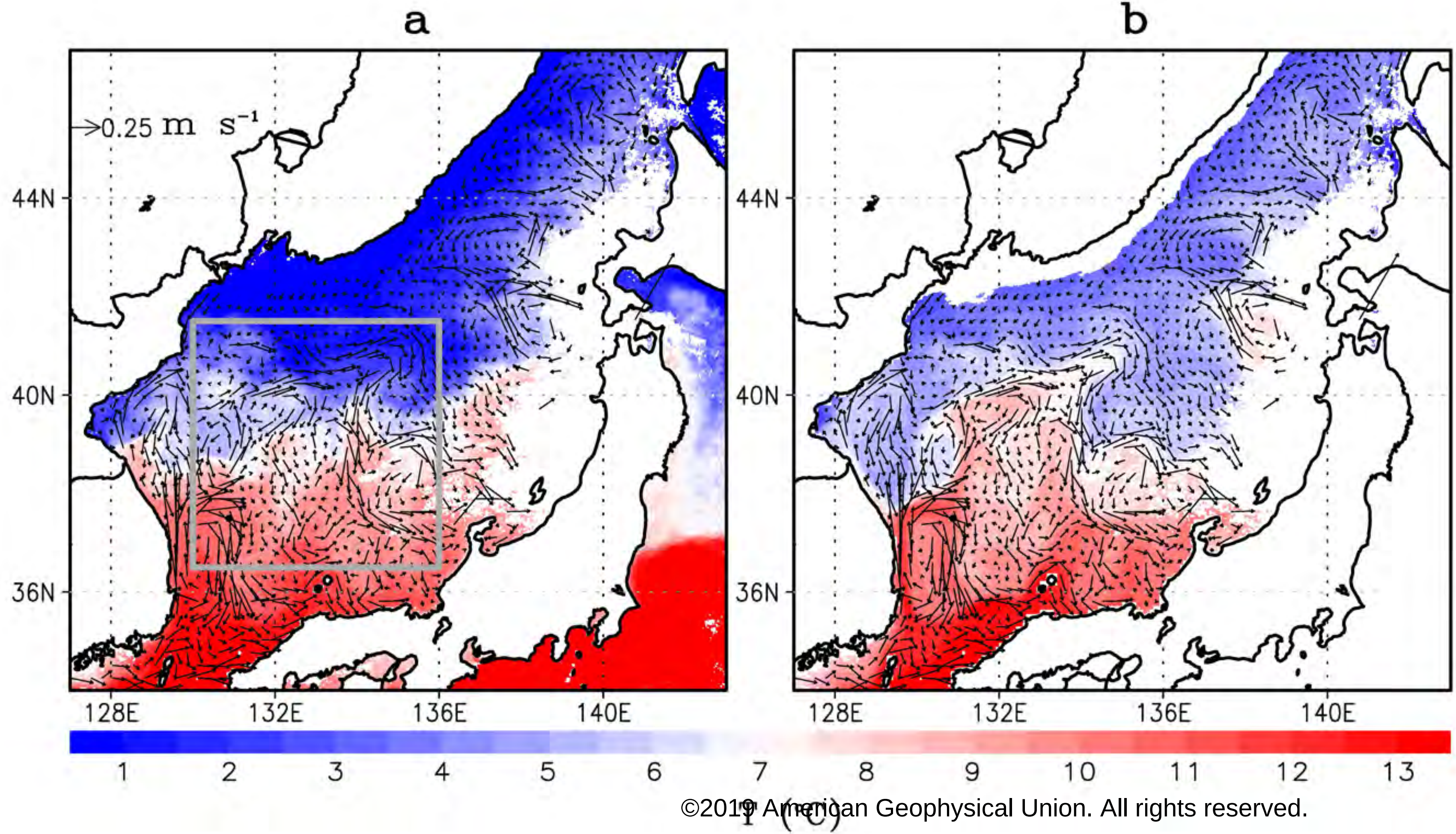
a
b
0.25 m s⁻¹
44N
40N
36N
128E
132E
136E
140E
1
2
3
4
5
6
7
8
9
10
11
12
13
T (°C)

fig2.

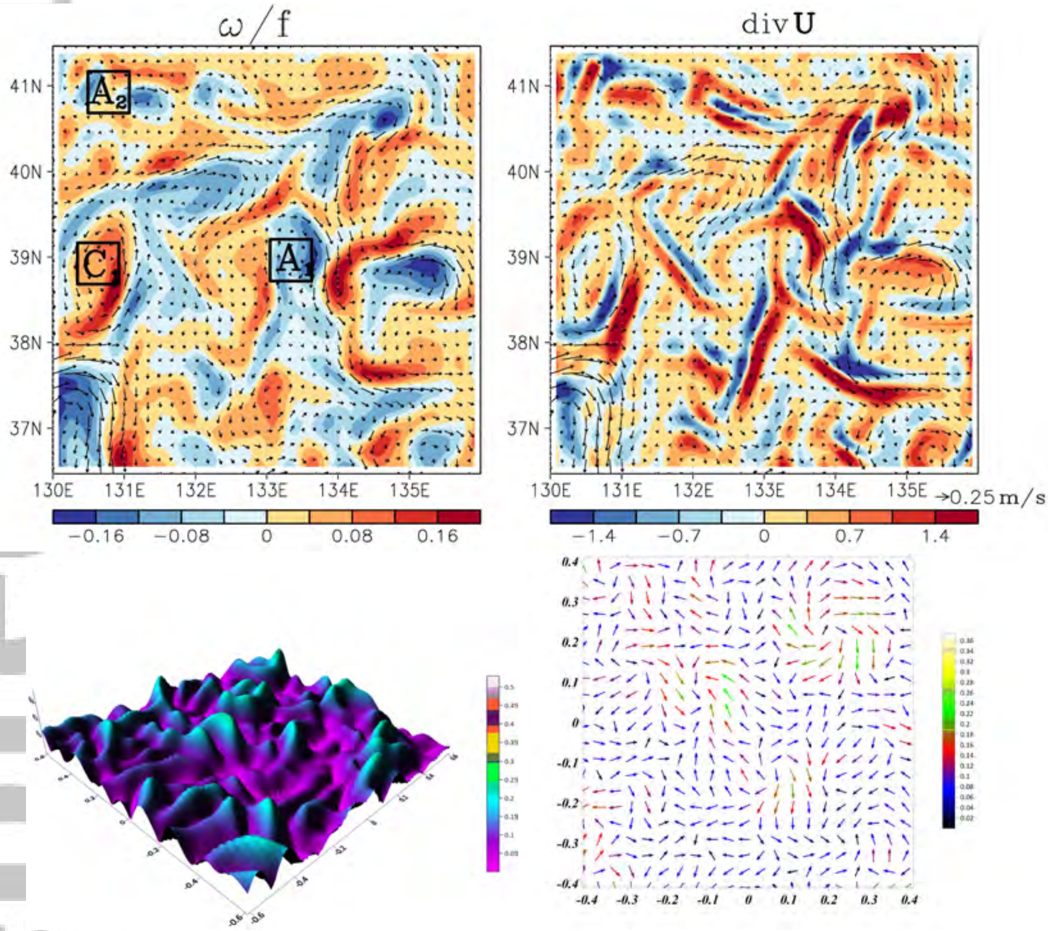

ω / f
div U
A2
C1
A1
41N
40N
39N
38N
37N
130E
131E
132E
133E
134E
135E
→0.25 m/s
−0.16
−0.08
0
0.08
0.16
−1.4
−0.7
0
0.7
1.4
0.4
0.3
0.2
0.1
0
-0.1
-0.2
-0.3
-0.4

fig3.

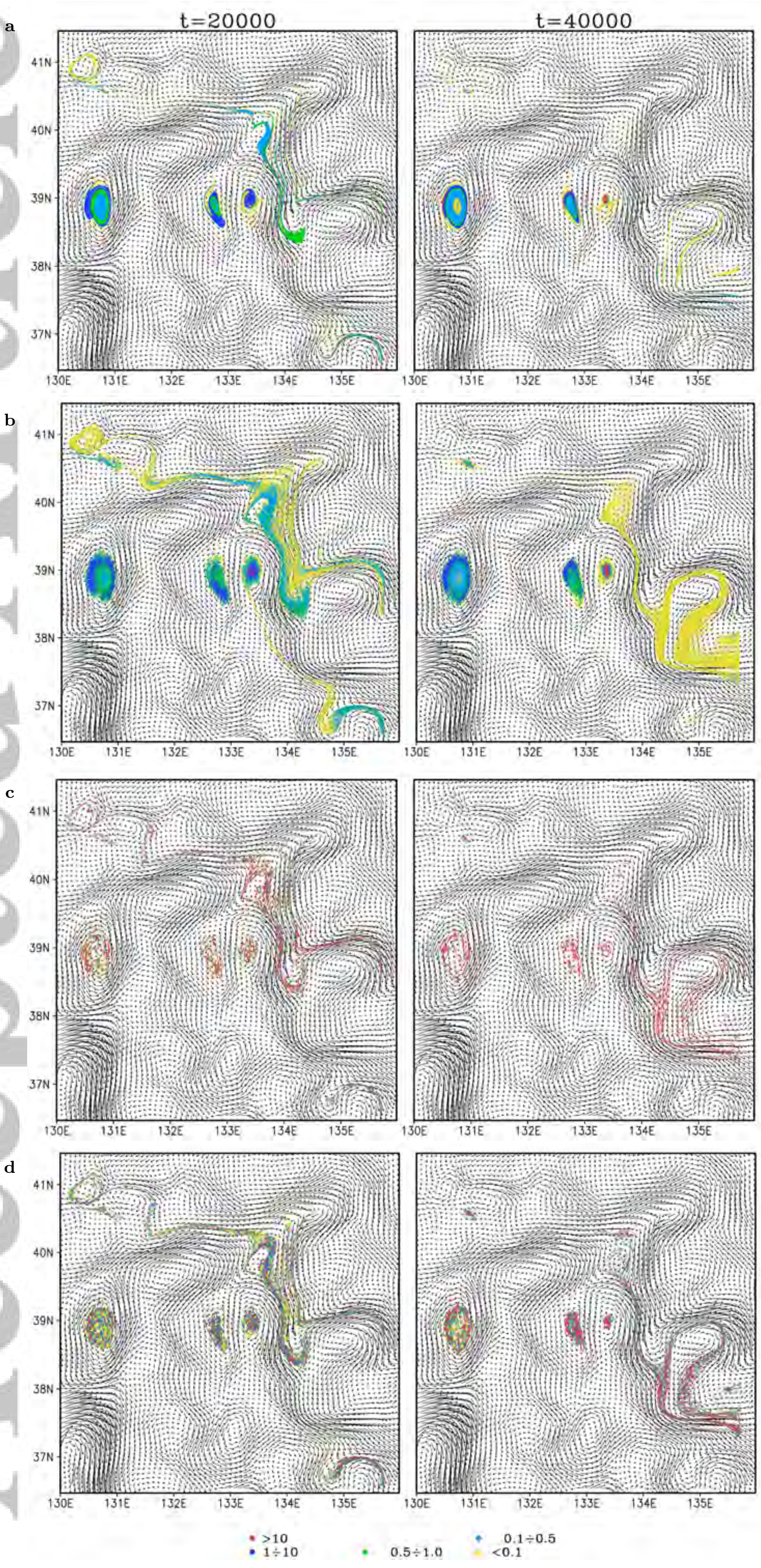
a
b
c
d
t=20000
t=40000
41N
40N
39N
38N
37N
130E
131E
132E
133E
134E
135E
>10
1÷10
0.5÷1.0
0.1÷0.5
<0.1

fig4.

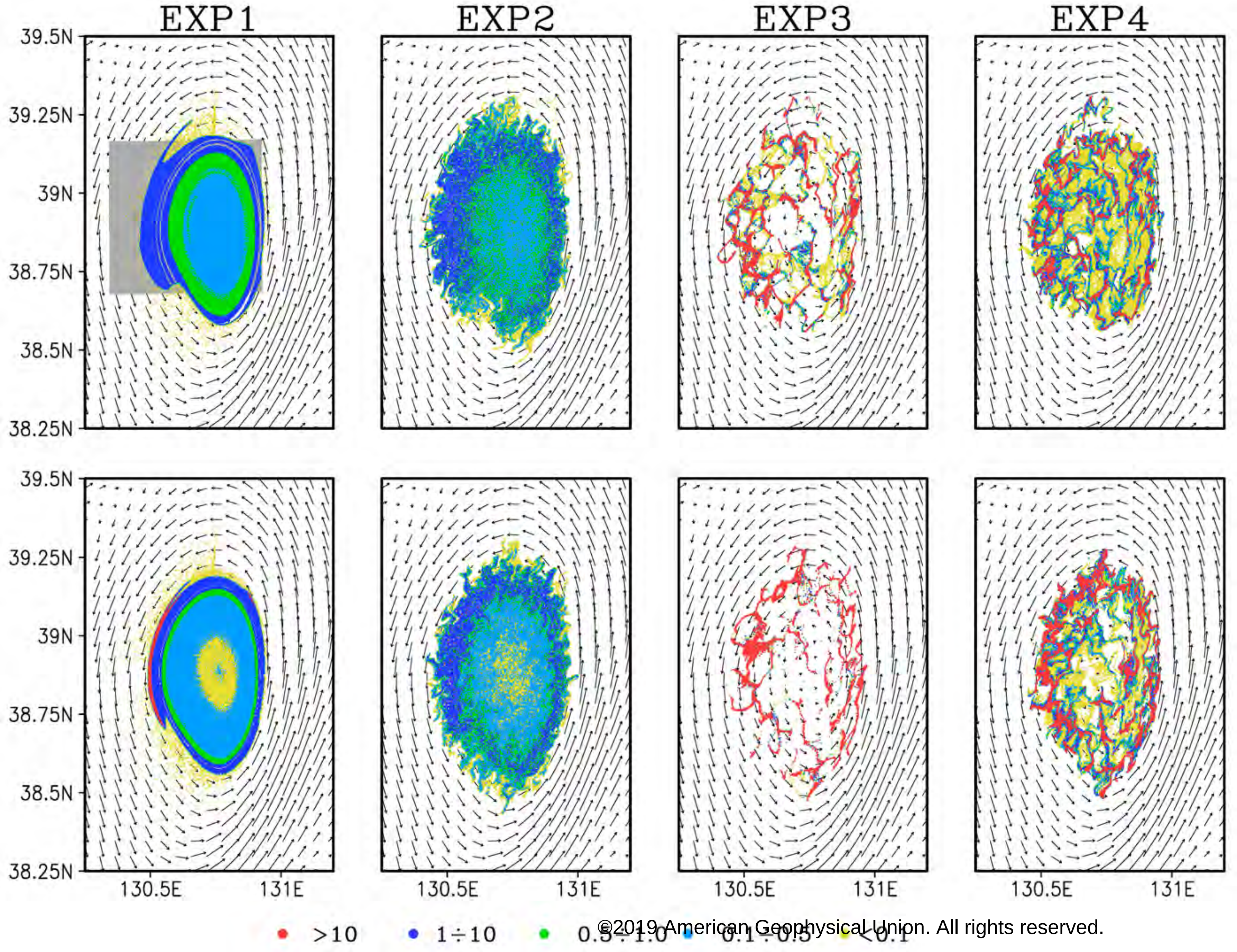
EXP1
EXP2
EXP3
EXP4
39.5N
39.25N
39N
38.75N
38.5N
38.25N
130.5E
131E
>10
1÷10
0.5÷1.0
0.1÷0.5
<0.1

fig5.

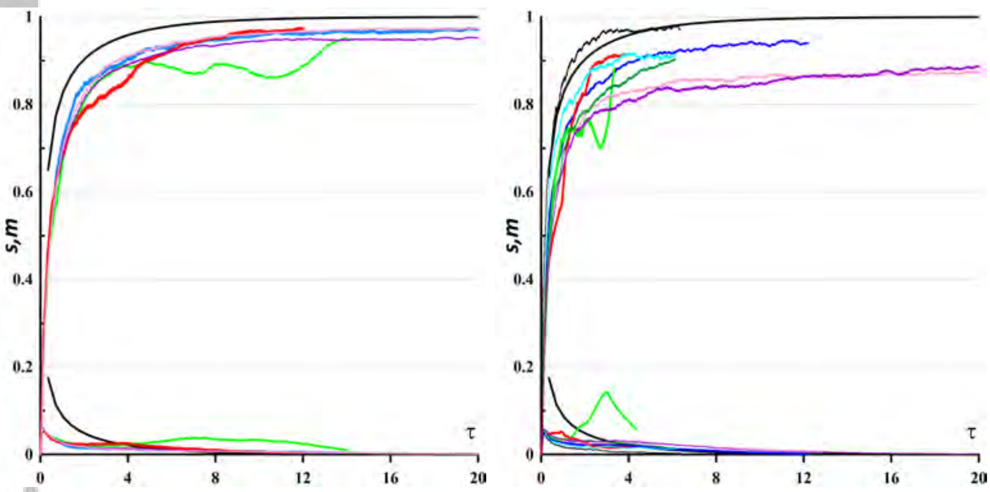
1
0.8
0.6
0.4
0.2
0
s,m
τ
0
4
8
12
16
20
1
0.8
0.6
0.4
0.2
0
s,m
τ
0
4
8
12
16
20